Monthly Notices of the ROYAL ASTRONOMICAL SOCIETY

MNRAS **463,** 604–614 (2016) doi:10.1093/mnras/stw1999
Advance Access publication 2016 August 11

Broad-band spectrophotometry of HAT-P-32 b: search for a scattering signature in the planetary spectrum

M. Mallonn,[1]★ I. Bernt,[1] E. Herrero,[2] S. Hoyer,[3,4] J. Kirk,[5] P. J. Wheatley,[5] M. Seeliger,[6] F. Mackebrandt,[1] C. von Essen,[7] K. G. Strassmeier,[1] T. Granzer,[1] A. Künstler,[1] V. S. Dhillon,[8,3] T. R. Marsh[5] and J. Gaitan[9]

[1]*Leibniz-Institut für Astrophysik Potsdam (AIP), An der Sternwarte 16, D-14482 Potsdam, Germany*
[2]*Institut de Ciències de l'Espai (CSIC-IEEC), Campus UAB, Carrer de Can Magrans s/n, E-08193 Cerdanyola del Vallès, Spain*
[3]*Instituto de Astrofísica de Canarias, Vía Láctea s/n, E-38205 La Laguna, Tenerife, Spain*
[4]*Departamento de Astrofísica, Universidad de La Laguna, E-38206 La Laguna, Tenerife, Spain*
[5]*Department of Physics, University of Warwick, Gibbet Hill Road, Coventry CV4 7AL, UK*
[6]*Astrophysical Institute and University Observatory Jena, Schillergäßchen 2-3, D-07745 Jena, Germany*
[7]*Stellar Astrophysics Centre (SAC), Department of Physics and Astronomy, Aarhus University, DK-8000 Aarhus C, Denmark*
[8]*Department of Physics and Astronomy, University of Sheffield, Sheffield S3 7RH, UK*
[9]*C/10 Violeta, E-17300 Blanes, Girona, Spain*

Accepted 2016 August 5. Received 2016 August 5; in original form 2016 May 12

ABSTRACT

Multicolour broad-band transit observations offer the opportunity to characterize the atmosphere of an extrasolar planet with small- to medium-sized telescopes. One of the most favourable targets is the hot Jupiter HAT-P-32 b. We combined 21 new transit observations of this planet with 36 previously published light curves for a homogeneous analysis of the broad-band transmission spectrum from the Sloan u' band to the Sloan z' band. Our results rule out cloud-free planetary atmosphere models of solar metallicity. Furthermore, a discrepancy at reddest wavelengths to previously published results makes a recent tentative detection of a scattering feature less likely. Instead, the available spectral measurements of HAT-P-32 b favour a completely flat spectrum from the near-UV to the near-IR. A plausible interpretation is a thick cloud cover at high altitudes.

Key words: techniques: photometric – planets and satellites: atmosphere – planets and satellites: individual: HAT-P-32 b.

1 INTRODUCTION

Transit events offer the opportunity to characterize the atmospheres of extrasolar planets. During a transit, a fraction of the star light shines through the outmost layers of the planetary atmosphere. Depending on the opacity of its chemical constitution, the star light transmits or becomes scattered or absorbed. Therefore, the altitude of optical depth equalling unity (effective planetary radius) is a function of wavelength and depends on the atmospheric composition. The measurement of the effective planetary radius as a function of wavelength is called transmission spectroscopy and is often accomplished by spectrophotometric observations of the transit event. The observer obtains photometric transit light curves at multiple wavelengths, either simultaneously by low-resolution spectroscopic observations (e.g. Bean, Miller-Ricci Kempton & Homeier 2010; Gibson et al. 2013a; Mallonn et al. 2015a) or in different broad-band filters both simultaneously (e.g. Mancini et al. 2013; Nascimbeni et al. 2013) or at multiple transit epochs (e.g. de Mooij et al. 2012; Dragomir et al. 2015; Mallonn et al. 2015b).

A value of the planetary radius in relation to the (wavelength-independent) stellar radius is derived by a model fit to the transit light curve. This method was successfully applied to measure the spectroscopic absorption feature of, e.g. sodium, potassium, and water (Sing et al. 2011b; Huitson et al. 2013; Nikolov et al. 2014). In other target spectra, the spectral features predicted by cloud-free models could be ruled out (e.g. Gibson et al. 2013a; Pont et al. 2013; Mallonn et al. 2015a; Lendl et al. 2016). These spectra are either simply flat in the probed wavelength region, or show a trend of increasing opacity towards blue wavelengths explainable by Rayleigh or Mie scattering (Jordán et al. 2013; Stevenson et al. 2014). Interestingly, at wavelengths shorter than about 500 nm currently all gas giants on close orbits (the so-called hot Jupiters) seem to show an increase in opacity when measured with sufficient precision (uncertainty of the effective planetary size about one scaleheight, Sing et al. 2016).

★ E-mail: mmallonn@aip.de

One target of special interest is the hot Jupiter HAT-P-32 b. It was discovered by Hartman et al. (2011) and is one of the best targets for transmission spectroscopy because of its large transit depth of more than 2 per cent, its large planetary scaleheight of about 1000 km, and a relatively bright host star ($V = 11.4$ mag). HAT-P-32 b's atmospheric transmission spectrum lacks the predicted cloud-free absorption of Na, K, and H_2O (assuming solar composition, Gibson et al. 2013b, hereafter G13). This result was recently confirmed by transmission spectroscopy of Nortmann et al. (2016, hereafter N16). However, Mallonn & Strassmeier (2016, hereafter Paper I) found indications for a slope of increasing effective planetary radius towards the blue by measuring the spectrum from 330 to 1000 nm. The amplitude of this increase of only two atmospheric pressure scaleheights is small compared to other hot Jupiters with measured scattering signatures, e.g. HD189733 b (Sing et al. 2011a; Pont et al. 2013). In this work, we attempt a verification of this blueward increase of effective planetary radius of HAT-P-32 by multi-epoch and multicolour observations using broad-band photometry.

While in principle the broad-band filters allow for low photon-noise in the photometry even with metre-sized telescopes, it has proven to be a demanding task to reach sufficient precision to discriminate between different models (e.g. Fukui et al. 2013; Teske et al. 2013; Mallonn et al. 2015b). Furthermore, for single observations per filter a potential effect of correlated noise is not always obvious (e.g. Southworth et al. 2012). One way to lower such potential effect is to observe multiple transit light curves per filter under the assumption that the correlated noise does not repeat because observing conditions change from night to night for ground-based observations (Lendl et al. 2013; Mallonn et al. 2015b). Therefore, we collected the largest sample of light curves analysed for broad-band spectrophotometry of an exoplanet so far. We present 21 new observations and analyse them homogeneously together with 36 already published light curves. Section 2 gives an overview about the observations and data reduction and Section 3 describes the analysis. The results are presented in Section 4 and discussed in Section 5. The conclusions follow in Section 6.

2 OBSERVATIONS AND DATA REDUCTION

Transit light curves were taken with the robotic 1.2 m STELLA telescope, with the 2.5 m Nordic Optical Telescope (NOT), the 0.8 m IAC80 telescope, the 2.2 m telescope of Calar Alto, the 70 cm telescope of the Leibniz Institute for Astrophysics Potsdam (AIP), and the 4.2 m William Herschel Telescope (WHT).

STELLA and its wide field imager WiFSIP (Strassmeier et al. 2004; Weber, Granzer & Strassmeier 2012) observed in total 11 transits in five observing seasons using the filters Johnson B and Sloan r'. The first seven transits were observed with both filters alternating. These r' band light curves were already published by Seeliger et al. (2014). The four light curves from 2014 to 2016 were taken only in Johnson B. WiFSIP holds a back-illuminated 4k × 4k 15 μm pixel CCD and offers a field of view (FoV) of 22 arcmin × 22 arcmin. To minimize the read-out time, a windowing of the CCD was used reducing the FoV to about 15 arcmin × 15 arcmin. A small defocus was applied to spread the point spread function to an artificial full width at half-maximum (FWHM) of about 3 arcsec.

One transit was observed with the NOT as a Fast Track program using ALFOSC in imaging mode. ALFOSC contains a 2k × 2k E2V CCD providing an FoV of 6.4 arcmin × 6.4 arcmin.

One transit was observed with BUSCA, the four-channel imager at the Calar Alto Observatory 2.2 m telescope (Reif et al. 1999). The instrument performs simultaneous photometry in four different bandpasses with an FoV of 11 arcmin × 11 arcmin. For the bandpass of shortest wavelength, we used a white glass filter and the beam splitter defined the limit of $\lambda < 430$ nm. For the other bandpasses from blue to red, we used a Thuan–Gunn g, Thuan–Gunn r, and Bessel I filter. Unfortunately, the observation of a pre-ingress baseline was lost due to weather, and the observing conditions remained to be non-photometric. We discarded the light curve of shortest wavelength because it exhibited significantly larger correlated noise than the other three light curves.

One transit was observed with the IAC80 telescope, owned and operated by the Instituto de Astrofísica de Canarias (IAC), using its wide field imager CAMELOT. It is equipped with a CCD-E2V detector of 2k × 2k, with a pixel scale of about 0.3 arcsec pixel^{-1} providing an FoV of about 10.5 arcmin × 10.5 arcmin.

Two transits were observed with the 70 cm telescope of the AIP, located in the city of Potsdam at the Babelsberg Observatory. The telescope is equipped with a cryogenic cooled 1k × 1k TEK-CCD providing an FoV of 8 arcmin × 8 arcmin. The first transit was observed in Johnson B and Johnson V quasi-simultaneously with alternating filters, the second one in Johnson V only. We applied a 3 × 3 pixel binning to reduce the detector read-out time.

Data of an additional transit were taken with the triple beam, frame-transfer CCD camera ULTRACAM (Dhillon et al. 2007) mounted at the WHT. The instrument optics allow for the simultaneous photometry in three different bandpasses. We chose the filters Sloan u', Sloan g', and a filter centred on the sodium doublet at 591.2 nm with a width (FWHM) of 31.2 nm. To avoid saturation of the brightest stars, the exposure time was extremely short with 0.3 s. However, the overheads are negligible owing to the frame-transfer technique. The detectors were read out in windowed mode. For the u' channel, 10 exposures were co-added on chip before read-out. In the analysis, we used the light curves binned in time. The g' band light curve showed correlated noise of ∼3 mmag on short time-scales and was excluded from the analysis.

We extended our sample of broad-band transit data by the five light curves published by Hartman et al. (2011) and 26 light curves published by Seeliger et al. (2014). Furthermore, we searched the Exoplanet Transit Database[1] (ETD; Poddaný, Brát & Pejcha 2010) for available amateur observations of sufficient quality to be helpful in the recent work. ETD performs online a simple transit fit, and we used its derived transit depth uncertainty and a visual inspection for selecting five light curves for our purposes. The characteristics of all light curves are summarized in Table 1.

The data reduction of all new light curves except the ULTRACAM data was done as described in our previous work on HAT-P-12 b (Mallonn et al. 2015b). Bias and flat-field correction was done in the standard way, with the bias value extracted from the overscan regions. We performed aperture photometry with the publicly available software SExtractor using the option of a fixed circular aperture MAG_APER. The set of comparison stars (flux sum) was chosen to minimize the root mean square (rms) of the light-curve residuals after subtraction of a second-order polynomial over time plus transit model using literature transit parameter. Using the same criterion of a minimized rms, we also determined and applied the best aperture width. A significant fraction of our light curves nearly reached photon-noise-limited precision. The transit light curves of 2012 October 12, observed simultaneously with the

[1] http://var2.astro.cz/ETD/

Table 1. Overview of the analysed transit observations of HAT-P-32 b. The columns give the observing date, the telescope used, the chosen filter, the airmass range of the observation, the exposure time, the observing cadence, the number of observed data points in-transit, the number of observed data points out-of-transit, the dispersion of the data points as rms of the observations after subtracting a transit model and a detrending function, the β factor (see Section 3), and the reference of the light curves.

Date	Telescope	Filter	$t_{\rm exp}$ (s)	Cadence (s)	$N_{\rm it}$	$N_{\rm oot}$	rms (mmag)	β	Reference
2007 September 24	FLWO 1.2 m	z'		33	330	273	1.93	1.13	Hartman et al. (2011)
2007 October 22	FLWO 1.2 m	z'		53	205	284	2.51	1.00	Hartman et al. (2011)
2007 November 06	FLWO 1.2 m	z'		28	386	373	2.06	1.00	Hartman et al. (2011)
2007 November 19	FLWO 1.2 m	z'		38	292	373	1.68	1.27	Hartman et al. (2011)
2007 December 04	FLWO 1.2 m	g'		33	322	274	1.85	1.00	Hartman et al. (2011)
2011 November 01	STELLA	B	30	115	95	45	1.96	1.04	This work
2011 November 01	STELLA	r'	15	115	92	41	1.90	1.00	Seeliger et al. (2014)
2011 November 14	Jena 0.6/0.9 m	R	40	63	174	126	1.76	1.04	Seeliger et al. (2014)
2011 November 29	STELLA	B	30	115	94	22	1.21	1.00	This work
2011 November 29	STELLA	r'	15	115	95	21	1.30	1.01	Seeliger et al. (2014)
2011 November 29	Babelsberg 70 cm	B	30	75	149	224	2.65	1.00	This work
2011 November 29	Babelsberg 70 cm	V	30	75	151	222	2.44	1.38	This work
2011 November 29	Rozhen 2.0 m	V	20	23	461	172	0.99	1.00	Seeliger et al. (2014)
2011 December 01	Rozhen 2.0 m	R	20	23	470	218	1.38	1.99	Seeliger et al. (2014)
2011 December 14	Rozhen 0.6 m	R	60	63	177	78	1.87	1.09	Seeliger et al. (2014)
2011 December 27	Rozhen 2.0 m	R	20	39	280	66	1.05	1.81	Seeliger et al. (2014)
2012 January 15	Swarthmore 0.6 m	R	50	59	184	169	3.21	1.00	Seeliger et al. (2014)
2012 August 15	Rozhen 2.0 m	R	25	44	252	93	1.24	1.00	Seeliger et al. (2014)
2012 August 17	STELLA	B	30	115	97	56	1.61	1.48	This work
2012 August 17	STELLA	r'	15	115	96	58	1.72	1.00	Seeliger et al. (2014)
2012 September 12	OSN 1.5 m	R	30	39	269	63	3.58	1.09	Seeliger et al. (2014)
2012 September 12	Trebur 1.2 m	R	50	59	182	84	2.02	1.23	Seeliger et al. (2014)
2012 September 14	OSN 1.5 m	R	30	40	278	181	1.23	1.58	Seeliger et al. (2014)
2012 October 12	WHT	Na I	14.7	14.7	678	928	0.99	1.77	This work
2012 October 12	WHT	u'	19.5	19.5	509	712	1.39	1.58	This work
2012 October 12	NOT	B	7.0	14.9	657	266	1.82	1.00	This work
2012 October 25	STELLA	B	25	105	104	55	2.35	1.00	This work
2012 October 25	STELLA	r'	25	105	105	54	2.48	1.03	Seeliger et al. (2014)
2012 October 31	SON 0.4 m	R		42	261	150	3.07	1.00	ETD, P. Kehusmaa
2012 November 07	0.25 m	V	180	190	53	24	2.23	1.00	ETD, J. Gaitan
2012 November 22	OSN 1.5 m	R	30	35	317	193	1.05	1.14	Seeliger et al. (2014)
2012 November 24	STELLA	B	40	136	79	60	2.57	1.00	This work
2012 November 24	STELLA	r'	25	136	77	62	2.60	1.00	Seeliger et al. (2014)
2012 December 05	Babelsberg 70 cm	V	30	36	315	303	2.41	1.53	This work
2012 December 22	STELLA	B	40	136	81	76	2.22	1.00	This work
2012 December 22	STELLA	r'	25	136	82	72	1.76	1.13	Seeliger et al. (2014)
2013 January 05	STELLA	B	40	136	81	77	1.48	1.23	This work
2013 January 05	STELLA	r'	25	136	82	76	1.32	1.12	Seeliger et al. (2014)
2013 August 22	0.35 m	R	70	87	127	84	2.03	1.04	ETD, V.P. Hentunen
2013 September 06	Rozhen 2.0 m	R	30	33	334	55	0.87	1.34	Seeliger et al. (2014)
2013 September 06	Jena 0.6/0.9 m	R	40	58	191	124	1.49	1.03	Seeliger et al. (2014)
2013 September 06	Torun 0.6 m	R	10	13	829	580	3.27	1.65	Seeliger et al. (2014)
2013 October 06	OSN 1.5 m	R	30	32	348	236	0.93	1.00	Seeliger et al. (2014)
2013 November 01	Rozhen 2.0 m	R	25	44	249	60	0.73	1.07	Seeliger et al. (2014)
2013 November 03	OSN 1.5 m	R	30	35	316	195	1.20	1.29	Seeliger et al. (2014)
2013 December 01	OSN 1.5 m	R	30	35	315	218	1.64	1.69	Seeliger et al. (2014)
2013 December 14	0.30 m	V		80	135	173	4.01	1.17	ETD, R. Naves
2013 December 29	Trebur 1.2 m	R	50	58	187	105	2.40	1.00	Seeliger et al. (2014)
2014 November 25	STELLA	B	60	94	117	61	1.44	1.25	This work
2014 December 21	Calar Alto 2.2 m	Gunn g	20	65	157	106	1.84	1.05	This work
2014 December 21	Calar Alto 2.2 m	Gunn r	20	65	160	107	1.39	1.10	This work
2014 December 21	Calar Alto 2.2 m	I	20	65	160	107	1.33	1.00	This work
2014 December 21	0.30 m	V		84	130	77	2.90	1.00	ETD, F. Campos
2015 January 05	STELLA	B	45	79	142	130	0.98	1.23	This work
2015 December 17	STELLA	B	45	79	139	77	1.73	1.47	This work
2015 December 30	IAC80	B	60	68	163	103	2.59	1.18	This work
2016 January 27	STELLA	B	45	79	142	67	1.89	1.56	This work

NOT and WHT, suffered from clouds moving through. We discarded all data points with flux levels below 50 per cent of its mean.

The ULTRACAM data were reduced in the same way as described in Kirk et al. (in preparation), using the ULTRACAM data reduction pipeline[2] with bias frames and flat-fields used in the standard way. Again, the aperture size used to perform aperture photometry was optimized to deliver the most stable photometry. Only two useful comparison stars were observed in the FoV, and a simple flux sum of both as reference was found to give the differential light curve of lowest scatter.

The 21 new light curves are shown in Fig. 1, and the 36 reanalysed literature light curves are presented in Fig. A1.

3 LIGHT-CURVE ANALYSIS

In this work, we model all transit light curves with the publicly available software JKTEBOP[3] (Southworth, Maxted & Smalley 2004; Southworth 2008) in version 34. It allows for a simultaneous fit of the transit model and a detrending function. Throughout this analysis, we use a second-order polynomial over time to detrend the individual light curves. The transit fit parameters consist of the sum of the fractional planetary and stellar radius, $r_\star + r_\mathrm{p}$, and their ratio $k = r_\mathrm{p}/r_\star$, the orbital inclination i, the transit mid-time T_0, the host-star limb-darkening coefficients (LDC) u and v of the quadratic limb-darkening law, and the coefficients $c_{0,1,2}$ of the polynomial over time. The index '$\star$' refers to the host star and 'p' refers to the planet. The dimensionless fractional radius is the absolute radius in units of the orbital semimajor axis a, $r_\star = R_\star/a$, and $r_\mathrm{p} = R_\mathrm{p}/a$. The planetary eccentricity is fixed to zero following Zhao et al. (2014) and the orbital period P_orb to 2.150 008 25 d according to Seeliger et al. (2014).

We modelled the stellar limb darkening with the quadratic, two-parameter law. Theoretical values for the LDC have been obtained by Claret, Hauschildt & Witte (2013) using the stellar parameter from Hartman et al. (2011) for the case of a circular planetary orbit. Following Southworth (2008) and our previous work on HAT-P-32 b in Paper I, we fitted for the linear LDC u and kept the quadratic LDC v fixed to its theoretical values, perturbing it by ± 0.1 on a flat distribution during the error estimation.

Following the same procedure as in Mallonn et al. (2015b), we begin the analysis of each light curve with an initial fit followed by a 3.5σ rejection of outliers. After a new transit model fit, we rescale the photometric uncertainties derived by SExtractor to yield a reduced χ^2 of unity for the light-curve residuals. Furthermore, we calculate the so-called β factor, a concept introduced by Gillon et al. (2006) and Winn et al. (2008) to include the contribution of correlated noise in the light-curve analysis. It describes the evolution of the standard deviation σ of the light-curve residuals when they become binned in comparison to Poisson noise. In the presence of correlated noise, σ of the binned residuals is larger by the factor β than with pure uncorrelated (white) noise. The value used here for each light curve is the average of the values for a binning from 10 to 30 min in 2 min steps. In the final transit fit, we fix the i and $r_\star$ to the values used in G13 and Paper I to achieve directly comparable values of k. We assume their uncertainties to be a common source of noise to all bandpasses, negligible in the search for relative variations of k over wavelength. Therefore, the derived errors on k are relative uncertainties. The free parameters per light curve have been r_p, u, and $c_{0,1,2}$. For the bandpasses with more than one light curve, we perform an individual fit per light curve, summarized in Table 2, and a joint run of all light curves per bandpass fitted simultaneously, summarized in Table 3. In the joint fit, the free parameters are r_p, u, and a set of detrending coefficients per involved light curve. Here, we added the Thuan–Gunn r light curve to the sample of r' data, and Thuan–Gunn g to the g' data because of significant overlap in the filter transmission curves. The k values of the individual and the joint fits are shown in Fig. 2.

The estimation of the transit parameter uncertainties was done with 'task 8' in JKTEBOP (Southworth et al. 2005), which is a Monte Carlo simulation, and with 'task 9' (Southworth 2008), which is a residual-permutation algorithm that takes correlated noise into account. We run the Monte Carlo simulation with 5000 steps. As final parameter uncertainties we adopted the larger value of both methods.

The time stamps from all light curves analysed in this work were transferred to $\mathrm{BJD_{TDB}}$ following the recommendation of Eastman, Siverd & Gaudi (2010). All individually derived transit mid-times of the light curves of our sample are in agreement with the ephemeris of Seeliger et al. (2014).

Adams et al. (2013) found a companion object only 2.9 arcsec to HAT-P-32, which was classified as a mid-M dwarf by Zhao et al. (2014). The flux of this object is fully included in the aperture used for the aperture photometry for all our light curves and dilutes the transit depth as third light contribution to the star–planet system. All values of k derived from r', R, I, and z' band light curves were corrected using equation 4 in Sing et al. (2011a) and the third light as a function of wavelength measured in Paper I.

In Paper I, we also measured and analysed the photometric variability of the host star and concluded that HAT-P-32 is photometrically constant without significant influence of stellar activity. Therefore, we assume there is no time dependence of k in the interval of our observations. We computed the reduced χ^2 value of k of the individual transits per filter versus the k value of the joint fit per filter and obtain the values of 4.2, 1.5, 1.7, and 2.4 for the bandpasses B, V, r', and R, respectively. These values are larger than unity and indicate underestimated individual error bars potentially caused by undetected correlated noise (Southworth et al. 2009; Southworth 2011). Therefore, we conservatively inflate the uncertainties of k of all individual light curves by the factor 1.5, which leads to an average reduced χ^2 of unity. The error bars of k of the joint fits per filter are in all cases the outcome of the residual-permutation algorithm, whose value decreases more conservatively with increasing number of light curves per joint fit than the uncertainty value derived by the Monte Carlo simulation.

4 RESULTS

4.1 Comparison to published spectra of HAT-P-32 b

The broad-band transmission spectrum of this work is shown in Fig. 3 together with previously published data of HAT-P-32 b. The results presented here are in very good agreement to the transmission spectra derived by G13 and N16 (note that N16 uses slightly different values for i and $r_\star$). There are small discrepancies to the results of Paper I. The B-band measurement differs by about 2σ, and the R-band value deviates by 2.5σ, whereas at all other wavelength there is an agreement within 1σ. All four investigations, G13, N16, Paper I, and this work show good consistency shortwards of ∼720 nm. At redder wavelengths of the Cousins I and Sloan z' band,

[2] http://deneb.astro.warwick.ac.uk/phsaap/software/ultracam/html/index.html

[3] http://www.astro.keele.ac.uk/jkt/codes/jktebop.html

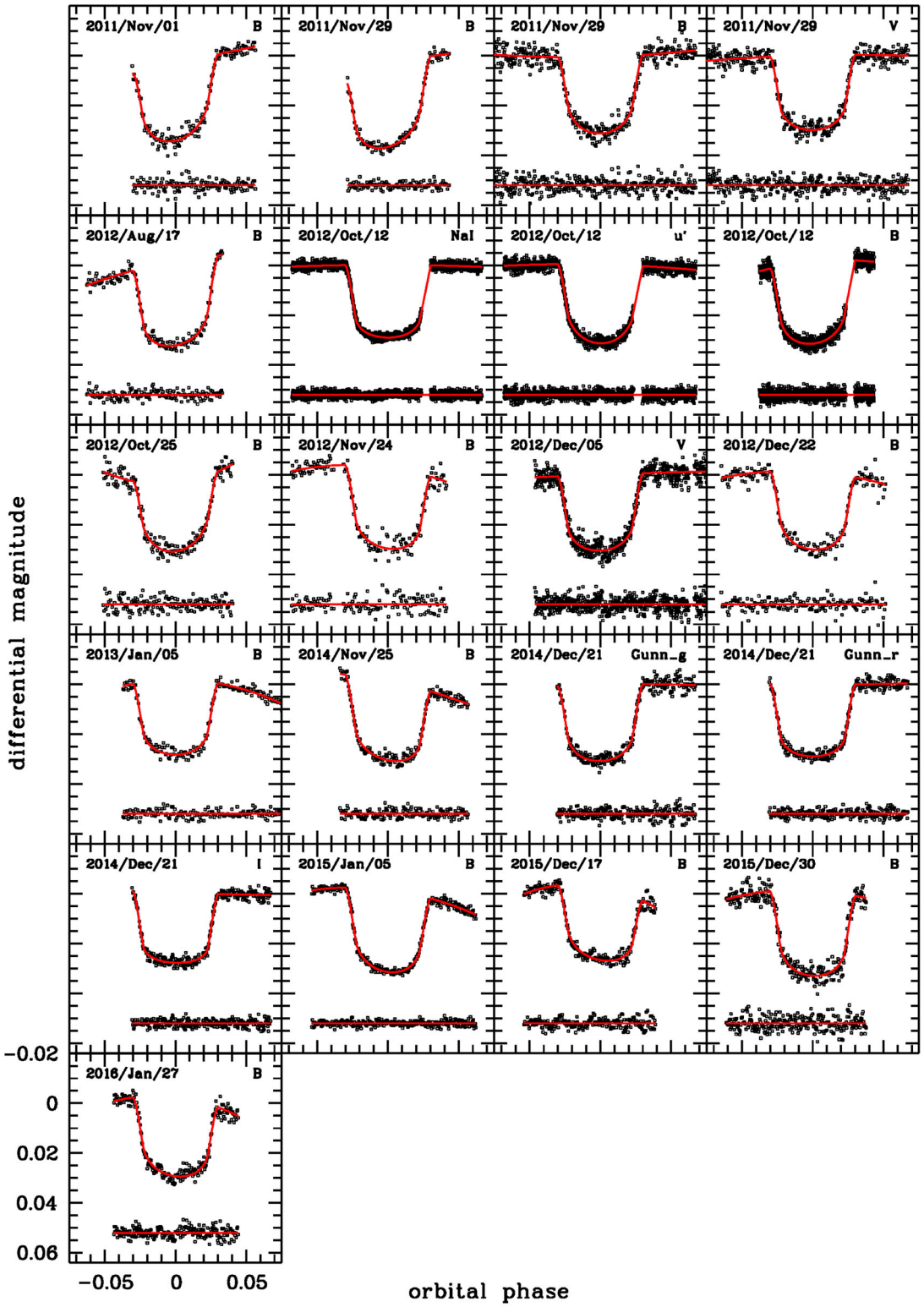

Figure 1. All light curves newly presented in this work. The red solid line denotes the individual best-fitting model, the resulting parameter values are given in Table 2. Below the light curves, their corresponding residuals are shown. The scale of all panels is identical with the tickmarks labelled in the lower left.

Table 2. Planet-to-star radius ratio k per observation with relative uncertainties. In Column 4, k is derived with u as free parameter, with the u value given in Column 5. The LDC v is fixed in the analysis to its theoretical value given in Column 7. The theoretical value of u is given in Column 6 for comparison. Column 8 gives the applied third-light correction of k.

Date	Telescope	Filter	k	$u_{\rm fit}$	$u_{\rm theo}$	$v_{\rm theo}$	$\Delta k_{\rm third\,light}$
2012 October 12	WHT	u'	0.1520 ± 0.0012	0.543 ± 0.023	0.696	0.112	0
2011 November 01	STELLA	B	0.1484 ± 0.0035	0.559 ± 0.038	0.583	0.208	0
2011 November 29	STELLA	B	0.1539 ± 0.0035	0.512 ± 0.017	0.583	0.208	0
2011 November 29	Babelsberg	B	0.1499 ± 0.0023	0.495 ± 0.022	0.583	0.208	0
2012 August 17	STELLA	B	$0.1589^{+0.0033}_{-0.0035}$	0.438 ± 0.058	0.583	0.208	0
2012 October 12	NOT	B	0.1556 ± 0.0019	0.486 ± 0.014	0.583	0.208	0
2012 October 25	STELLA	B	0.1404 ± 0.0043	0.535 ± 0.020	0.583	0.208	0
2012 November 24	STELLA	B	0.1559 ± 0.0040	0.435 ± 0.059	0.583	0.208	0
2012 December 22	STELLA	B	$0.1515^{+0.0031}_{-0.0029}$	0.479 ± 0.041	0.583	0.208	0
2013 January 05	STELLA	B	$0.1501^{+0.0026}_{-0.0028}$	0.430 ± 0.053	0.583	0.208	0
2014 November 25	STELLA	B	$0.1554^{+0.0026}_{-0.0025}$	0.400 ± 0.040	0.583	0.208	0
2015 January 05	STELLA	B	0.1556 ± 0.0013	0.484 ± 0.017	0.583	0.208	0
2015 December 17	STELLA	B	0.1465 ± 0.0039	0.514 ± 0.051	0.583	0.208	0
2015 December 30	IAC80	B	0.1601 ± 0.0032	0.440 ± 0.037	0.583	0.208	0
2016 January 27	STELLA	B	0.1526 ± 0.0056	0.492 ± 0.063	0.583	0.208	0
2007 December 04	FLWO 1.2 m	g'	$0.1536^{+0.0015}_{-0.0014}$	0.465 ± 0.018	0.545	0.205	0
2014 December 21	Calar Alto	Gunn g	$0.1524^{+0.0025}_{-0.0023}$	0.400 ± 0.021	0.518	0.221	0
2011 November 29	Rozhen 2.0 m	V	0.1527 ± 0.0010	0.395 ± 0.014	0.458	0.229	0
2011 November 29	Babelsberg	V	$0.1490^{+0.0029}_{-0.0027}$	0.463 ± 0.035	0.458	0.229	0
2012 November 07	0.25 m	V	0.1513 ± 0.0058	0.397 ± 0.046	0.458	0.229	0
2012 December 05	Babelsberg	V	0.1498 ± 0.0028	0.476 ± 0.049	0.458	0.229	0
2013 December 14	0.30 m	V	0.1471 ± 0.0058	0.240 ± 0.070	0.458	0.229	0
2014 December 21	0.30 m	V	$0.1548^{+0.0042}_{-0.0038}$	0.298 ± 0.029	0.458	0.229	0
2012 October 12	WHT	Na I	0.1514 ± 0.0011	0.297 ± 0.021	0.421	0.237	0.0001
2011 November 01	STELLA	r'	0.1502 ± 0.0033	0.331 ± 0.045	0.401	0.227	0.0001
2011 November 29	STELLA	r'	0.1561 ± 0.0037	0.293 ± 0.031	0.401	0.227	0.0001
2012 August 17	STELLA	r'	0.1534 ± 0.0023	0.361 ± 0.024	0.401	0.227	0.0001
2012 October 25	STELLA	r'	$0.1460^{+0.0046}_{-0.0048}$	0.315 ± 0.064	0.401	0.227	0.0001
2012 November 24	STELLA	r'	0.1518 ± 0.0042	0.296 ± 0.067	0.401	0.227	0.0001
2012 December 22	STELLA	r'	0.1550 ± 0.0039	0.274 ± 0.055	0.401	0.227	0.0001
2013 January 05	STELLA	r'	0.1537 ± 0.0022	0.319 ± 0.043	0.401	0.227	0.0001
2014 December 21	Calar Alto	Gunn r	0.1502 ± 0.0017	0.310 ± 0.020	0.361	0.238	0.0001
2011 November 14	Jena 0.6/0.9 m	R	0.1528 ± 0.0022	0.349 ± 0.021	0.387	0.219	0.0002
2011 December 01	Rozhen 2.0 m	R	0.1521 ± 0.0036	0.377 ± 0.036	0.387	0.219	0.0002
2011 December 14	Rozhen 0.6 m	R	0.1546 ± 0.0035	0.376 ± 0.014	0.387	0.219	0.0002
2011 December 27	Rozhen 2.0 m	R	$0.1546^{+0.0039}_{-0.0042}$	0.371 ± 0.032	0.387	0.219	0.0002
2012 January 15	Swarthmore	R	$0.1554^{+0.0027}_{-0.0025}$	0.267 ± 0.032	0.387	0.219	0.0002
2012 August 15	Rozhen 2.0 m	R	0.1499 ± 0.0021	0.315 ± 0.013	0.387	0.219	0.0002
2012 September 12	OSN 1.5 m	R	0.1602 ± 0.0088	0.294 ± 0.019	0.387	0.219	0.0002
2012 September 12	Trebur 1.2 m	R	0.1580 ± 0.0035	0.325 ± 0.039	0.387	0.219	0.0002
2012 September 14	OSN 1.5 m	R	$0.1523^{+0.0020}_{-0.0021}$	0.342 ± 0.018	0.387	0.219	0.0002
2012 October 31	SON 0.4 m	R	$0.1527^{+0.0034}_{-0.0031}$	0.365 ± 0.036	0.387	0.219	0.0002
2012 November 22	OSN 1.5 m	R	0.1493 ± 0.0013	0.291 ± 0.010	0.387	0.219	0.0002
2013 August 22	0.35 m	R	$0.1488^{+0.0029}_{-0.0033}$	0.412 ± 0.033	0.387	0.219	0.0002
2013 September 06	Rozhen 2.0 m	R	0.1508 ± 0.0029	0.277 ± 0.022	0.387	0.219	0.0002
2013 September 06	Jena 0.6/0.9 m	R	0.1514 ± 0.0018	0.312 ± 0.016	0.387	0.219	0.0002
2013 September 06	Torun 0.6 m	R	0.1484 ± 0.0030	0.278 ± 0.037	0.387	0.219	0.0002
2013 October 06	OSN 1.5 m	R	0.1492 ± 0.0009	0.344 ± 0.012	0.387	0.219	0.0002
2013 November 01	Rozhen 2.0 m	R	0.1534 ± 0.0015	0.309 ± 0.012	0.387	0.219	0.0002
2013 November 03	OSN 1.5 m	R	$0.1519^{+0.0014}_{-0.0016}$	0.276 ± 0.027	0.387	0.219	0.0002
2013 December 01	OSN 1.5 m	R	0.1498 ± 0.0025	0.287 ± 0.027	0.387	0.219	0.0002
2013 December 29	Trebur 1.2 m	R	0.1489 ± 0.0032	0.330 ± 0.031	0.387	0.219	0.0002

Table 2 – *continued*

Date	Telescope	Filter	k	$u_{\rm fit}$	$u_{\rm theo}$	$v_{\rm theo}$	$\Delta k_{\rm third\ light}$
2014 December 21	Calar Alto	I	$0.1514\ ^{+\ 0.0016}_{-\ 0.0015}$	0.227 ± 0.017	0.306	0.212	0.0007
2007 September 24	FLWO 1.2 m	z'	$0.1530\ ^{+\ 0.0018}_{-\ 0.0016}$	0.188 ± 0.021	0.265	0.211	0.0012
2007 October 22	FLWO 1.2 m	z'	$0.1481\ ^{+\ 0.0019}_{-\ 0.0018}$	0.219 ± 0.025	0.265	0.211	0.0012
2007 November 06	FLWO 1.2 m	z'	$0.1533\ ^{+\ 0.0012}_{-\ 0.0013}$	0.188 ± 0.017	0.265	0.211	0.0012
2007 November 19	FLWO 1.2 m	z'	0.1523 ± 0.0015	0.231 ± 0.036	0.265	0.211	0.0012

Table 3. Planet-to-star radius ratio k per filter with relative uncertainties.

Filter	k	$u_{\rm fit}$	$u_{\rm theo}$	$v_{\rm theo}$	$\Delta k_{\rm third\ light}$
u'	$0.152\ 04\ ^{+\ 0.001\ 18}_{-\ 0.001\ 23}$	0.543 ± 0.023	0.696	0.112	0
B	$0.153\ 38\ ^{+\ 0.000\ 73}_{-\ 0.000\ 82}$	0.502 ± 0.013	0.583	0.208	0
g' + Gunn g	$0.153\ 04\ ^{+\ 0.001\ 11}_{-\ 0.001\ 01}$	0.448 ± 0.022	0.535	0.214	0
V	$0.152\ 23\ ^{+\ 0.001\ 23}_{-\ 0.001\ 28}$	0.398 ± 0.014	0.458	0.229	0
Na I	$0.151\ 42\ ^{+\ 0.001\ 08}_{-\ 0.001\ 05}$	0.297 ± 0.021	0.421	0.237	0.000 06
r'+ Gunn r	$0.152\ 16\ ^{+\ 0.000\ 80}_{-\ 0.000\ 78}$	0.317 ± 0.016	0.392	0.230	0.000 07
R	$0.150\ 71\ ^{+\ 0.000\ 53}_{-\ 0.000\ 57}$	0.315 ± 0.010	0.387	0.219	0.000 21
I	$0.151\ 41\ ^{+\ 0.001\ 55}_{-\ 0.001\ 47}$	0.227 ± 0.017	0.306	0.212	0.000 69
z'	$0.151\ 49\ ^{+\ 0.000\ 73}_{-\ 0.000\ 78}$	0.221 ± 0.017	0.265	0.211	0.001 15

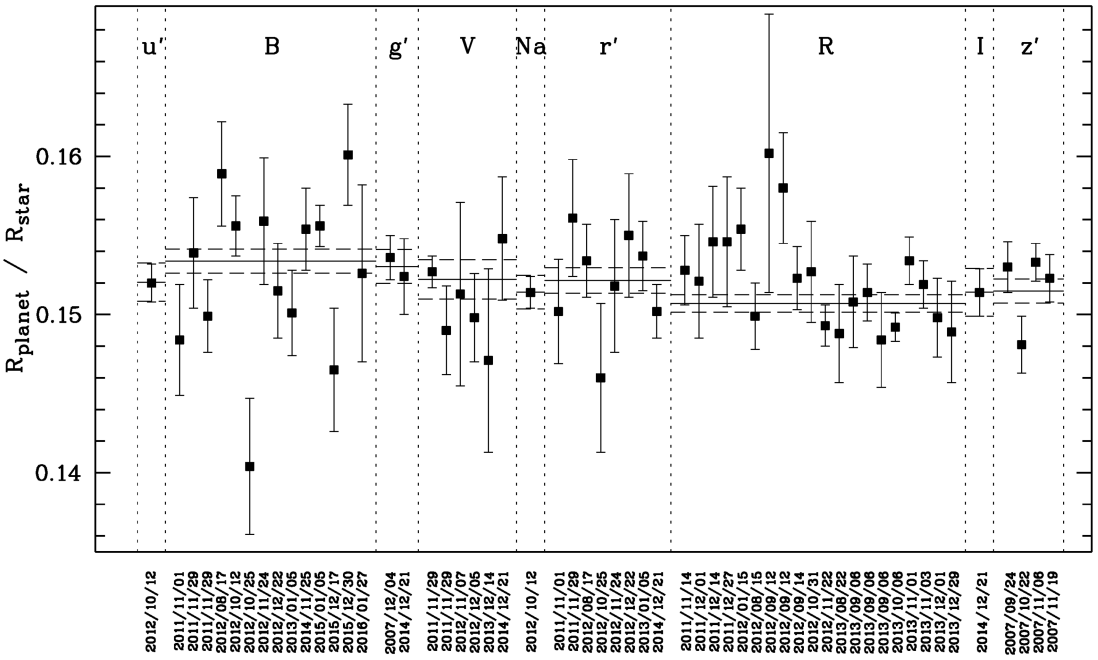

Figure 2. Planet–star radius ratio k for the 57 individual transit light curves in the same order as in Table 2. The horizontal lines mark the k value for the joint fit of all light curves per filter with their uncertainties given by the horizontal dashed lines.

Paper I deviates from the other three in exhibiting lower values of k of about one scaleheight. We experimented again with the LDC by fixing u and v in the analysis to the values derived in the three previous publications and found that the deviation of k in Paper I cannot be explained by the slight discrepancies in the LDC. Instead, a potential origin of the deviations are systematics in the light curves of Paper I.

4.2 Treatment of stellar limb darkening

The treatment of limb darkening in the modelling of exoplanet transit light curves is a debated topic. Multiple stellar limb-darkening laws exist in varying complexity with the two-parameter, quadratic law as the one with broadest application. The LDC u and v can be either included in the fitting process as free parameters (as suggested by, e.g. Csizmadia et al. 2013) or fixed to theoretical values (e.g.

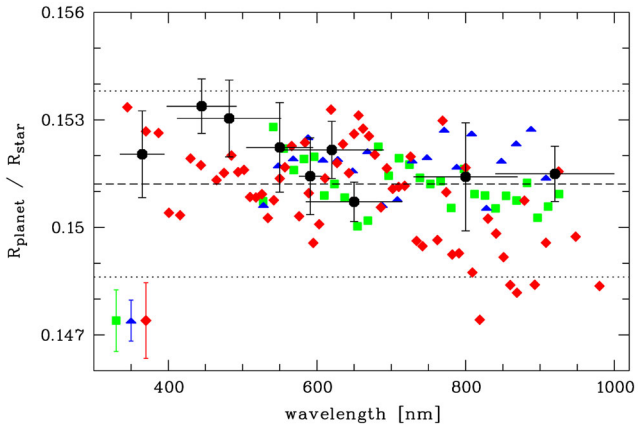

Figure 3. Broad-band transmission spectrum of HAT-P-32 b. This work is shown in black circles, horizontal bars indicate the width of the corresponding filter curve. Spectra published by G13 (green rectangular), N16 (blue triangle), and Paper I (red diamond) are shown for comparison. The average uncertainties of G13, N16, and Paper I are presented in the lower left. The dotted horizontal lines indicate plus and minus two scaleheights of the mean value.

Claret et al. 2013). Both options include advantages and disadvantages (see e.g. Müller et al. 2013). Therefore, Southworth (2008) introduced an intermediate solution by fitting for the linear LDC u while keeping the quadratic LDC v fixed to theoretical values for the quadratic limb-darkening law. We used this option here and in Paper I, finding in both a significant discrepancy between the fitted value of u and its theoretical value from Claret et al. (2013). For the majority of transiting exoplanet host stars, the measured LDC agree reasonably well to their theoretical predictions (Müller et al. 2013). However, another known exception is HD 209458 (Knutson et al. 2007; Claret 2009).

We repeated our analysis of the light curves of HAT-P-32 b by (i) keeping both LDC fixed to theoretical values of Claret et al. (2013) and (ii) fitting for both u and v in the light curve fit. The results are shown in Fig. 4. While option (i) results in a poorer fit and a general offset in planet–star radius ratio k towards lower values, there is a very good agreement when both u and v were free-to-fit compared to u free and v fix. However, the relative variation of k over wavelength remains nearly the same, irrespective of the treatment of the limb darkening. We verified this result further by the usage of the logarithmic limb-darkening law suggested by Espinoza & Jordán (2016) for the stellar temperature of HAT-P-32 and by the usage of the four-parameter law introduced by Claret (2000). The resulting values of k over wavelength remain nearly unaffected by the choice of the limb-darkening law, the same holds for the discrepancy when the LDC are free or fixed in the fit. Nevertheless, the treatment of the LDC affects the spectral slope. A fit of a linear regression results in a slight increase of k towards shorter wavelengths for free LDC, while the slope is nearly zero in the versions of fixed LDC (Fig. 4). However, in agreement to G13, N16, and Paper I, we consider the version of free LDC more reliable because of a better fit for all bandpasses. We note that using the theoretical LDC would reduce the agreement of the data with atmosphere models containing an enhanced opacity at short wavelengths (see Section 4.3). Therefore, it would not contradict the outcome of this work. We continue with the results obtained with free LDC.

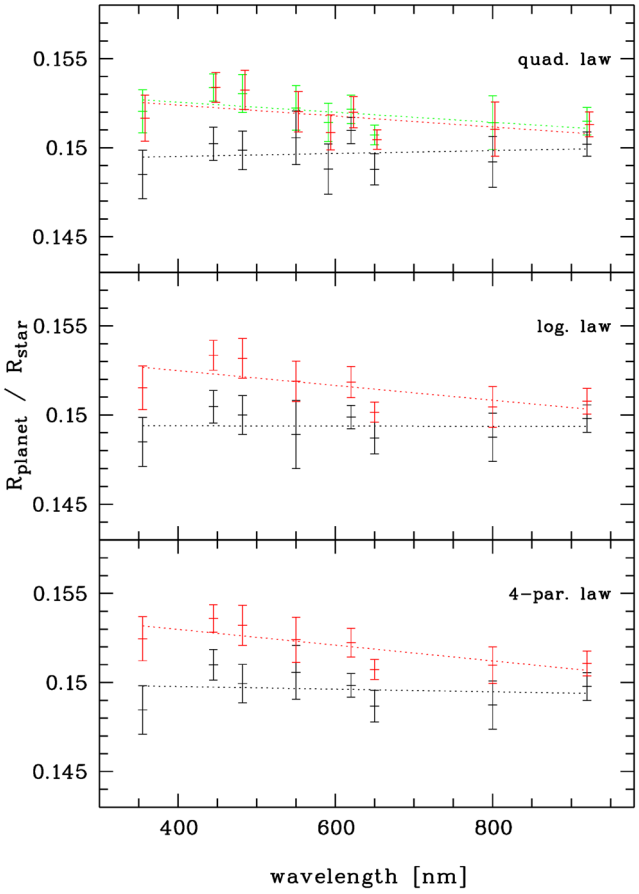

Figure 4. Planet–star radius ratio over wavelength of HAT-P-32 b derived by the usage of different stellar limb-darkening laws. Different colours denote different treatment of the LDC. Upper panel: quadratic stellar limb-darkening law. Black shows the k values for both LDC fixed to theoretical values, red denotes both LDC fitted, and green linear LDC fitted, but quadratic LDC fixed. Middle panel: logarithmic stellar limb-darkening law. Black denotes both LDC fixed, red implies both LDC fitted. Lower panel: four-parameter stellar limb-darkening law. Black denotes all four LDC fixed, red implies first LDC fitted, the other three fixed. All dotted lines show a linear regression corresponding to the data points of same colour.

4.3 Comparison to theoretical models

We compared the derived spectrophotometric transmission spectrum of this work with theoretical models that were supplied by Fortney et al. (2010) and calculated for HAT-P-32 b (see Fig. 5). The only fitted parameter is a vertical offset. For each model, we calculated the χ^2 value and the probability P of the χ^2 test, i.e. the probability that the measurements could result by chance if the model represented the true planetary spectrum. The values are summarized in Table 4. A cloud-free solar-composition model dominated by TiO absorption and a solar-composition model with TiO artificially removed are ruled out by the nine data points of this work, in agreement to results of G13, N16 and Paper I. Looking specifically at the theoretically predicted, prominent sodium D line, the data point from the ULTRACAM filter shows no extra absorption in agreement to the three previous studies. A model of solar composition without TiO including a Rayleigh-scattering component with a cross-section 100× that of molecular hydrogen yields $\chi^2 = 7.3$ for eight degrees of freedom (DOF), indicating good agreement between model and data. Similarly, a wavelength-independent planet–star radius ratio (flat spectrum) also yields an acceptable fit.

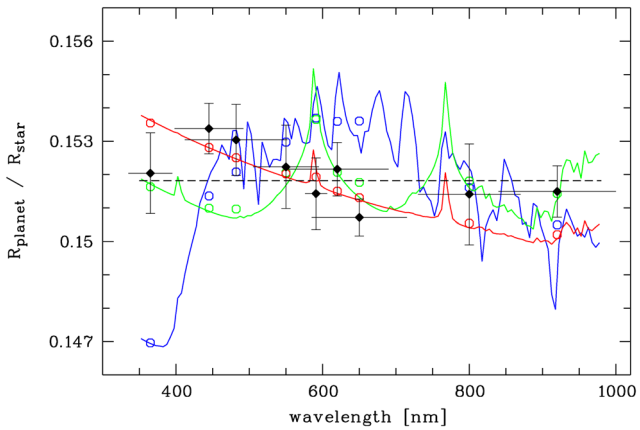

Figure 5. Broad-band transmission spectrum of HAT-P-32 b. The measured values of this work are given in black, horizontal bars show the width of the corresponding filter curve. Overplotted are a cloud-free solar-composition model of 1750 K (blue line), a cloud-free solar composition model of 1750 K without TiO (green line), and a solar composition model of 1750 K including H_2 Rayleigh scattering increased by a factor of 100 (red line, Fortney et al. 2010).The colour-coded open circles show the bandpass-integrated theoretical values.

Therefore, the measurements of this work cannot distinguish between the Rayleigh model and the flat model.

We attempt a combined comparison of the results derived here and in Paper I to the theoretical models, justified by the homogeneity of both analyses. Because of the deviating red data points of Paper I mentioned above, we restrict the wavelength range of these data to $\lambda < 720$ nm. The values of χ^2 and P are given in Table 4. This combined data set shows only a very low probability for a Rayleigh slope of 0.017, whereas a flat line is significantly favoured. The low-amplitude scattering slope proposed in Paper I also yields a good fit ($\chi^2 = 50.7$, DOF $= 48$), though of lower quality than the flat line.

For another test, we merge the measurements of all four studies G13, N16, Paper I, and this work, and compute a regression line. For simplicity and to account for inhomogeneities in the analyses, all data points were given equal weight. The resulting slope is $(-3.28 \pm 0.65) \times 10^{-6}$ nm^{-1}. However, excluding the data points $\lambda > 720$ nm of Paper I results in a weaker, insignificant slope of $(-1.16 \pm 0.60) \times 10^{-6}$ nm^{-1}, which means a consistency of the planet–star radius ratio between 350 and 1000 nm to within half of a scaleheight. A homogeneous re-analysis of all available data sets of HAT-P-32 b would be needed to reliably explore the potential slope at this sub-scaleheight precision.

5 DISCUSSION

A flat spectrum of a hot Jupiter exoplanet could be explained by a thick cloud layer at high altitudes acting as a grey absorber. A comparable case of a cloudy atmosphere is the hot Jupiter WASP-31 b with a cloud deck at only 1 mbar (Sing et al. 2015), and the super-Earth GJ1214b, whose transmission spectrum is featureless (Kreidberg et al. 2014) without measurable indications for scattering at blue wavelengths (de Mooij et al. 2013; Nascimbeni et al. 2015). In the presence of brightness inhomogeneities on the stellar surface, a flat spectrum could also be produced by the interplay of scattering in the planetary atmosphere and bright plage regions not occulted by the transiting planet (Oshagh et al. 2014). However, in Paper I we discuss this scenario to be very unlikely.

The results of this work indicate a flat spectrum with a spectral gradient of lower amplitude than two scaleheights. Interestingly, the near-UV/optical measurements of Sing et al. (2016) made with Hubble Space Telescope (HST)/STIS show no hot Jupiter spectrum without a blueward gradient. Each of the 10 investigated objects exhibit an increase in k from the z' band to the u' band of at least $\sim$ two, and up to $\sim$ six scaleheights. Therefore, HAT-P-32 b could be the hot Jupiter with the flattest spectrum measured so far. One way to confirm this result would be a homogeneous re-analysis of the published GEMINI, GTC, and LBT ground-based transit observations or new HST measurements at near-UV and optical wavelengths with STIS. Extrapolating from the optical spectrum, we would expect a muted or absent water feature at 1.4 μm. It would be very interesting to verify this prediction with HST/WFC3 measurements. If confirmed, HAT-P-32 b would strengthen the tentative correlation between cloud occurrence at high altitudes and a low planetary surface gravity found by Stevenson (2016).

6 CONCLUSIONS

HAT-P-32 b is one of the most favourable targets for transmission spectroscopy in terms of host star brightness and predicted amplitude of the potential transmission signal. In Paper I, we obtained a transmission spectrum from 330 to 1000 nm showing a tentative increase of the planet–star radius ratio towards blue wavelength of low amplitude. In this work, we collected the largest sample of broad-band transit photometry used for spectrophotometry so far to follow-up on this slope in the planetary spectrum. The light curves were taken in nine different filters from Sloan u' over several Johnson bands and one specific filter centred at the Na I D line to the Sloan z' band. The resulting spectrum was independent of the choice of the stellar limb-darkening law in the analysis. However, the spectral gradient was dependent on the treatment of the LDC in the fit. We advocate the inclusion of the linear coefficient as a free parameter in the light-curve modelling because it resulted in a better fit in all bandpasses.

While the new measurements of this work were of sufficient precision to rule out clear atmosphere models with solar metallicity, they could not distinguish between a Rayleigh-slope model and a wavelength-independent planet–star radius ratio. However, the new data helped to verify the proposed spectral gradient in showing that the k values redward of 720 nm of Paper I might be too low by about one scaleheight, potentially caused by systematics in the

Table 4. Fit statistics of theoretical models against the derived transmission spectrum.

	This work			This work and Paper I, $\lambda < 720$ nm		
Models	χ^2	N, DOF	P	χ^2	N, DOF	P
Solar composition, clear	62.9	9, 8	$\ll$0.001	219.6	49, 48	$\ll$0.001
Solar composition, without TiO, clear	21.9	9, 8	0.005	106.2	49, 48	$\ll$0.001
Rayleigh	7.6	9, 8	0.50	70.9	49, 48	0.017
Flat	10.3	9, 8	0.24	43.8	49, 48	0.65

measurements. Excluding these data favoured a spectrum that is flat over the entire wavelength range. HAT-P-32 b might be the hot Jupiter with the flattest spectrum observed so far. However, we suggest the combination of the currently available ground-based data by a homogeneous re-analysis, and the performance of transit observations with HST/STIS to confirm this peculiar result.

ACKNOWLEDGEMENTS

This article is based on observations made with the STELLA robotic telescopes in Tenerife, an AIP facility jointly operated by AIP and IAC, the IAC80 telescope operated on the island of Tenerife by IAC in the Spanish Observatorio del Teide, the Nordic Optical Telescope, operated by the Nordic Optical Telescope Scientific Association at the Observatorio del Roque de los Muchachos, La Palma, Spain, of the IAC, the William Herschel Telescope, operated by the Isaac Newton Group and run by the Royal Greenwich Observatory at the Spanish Roque de los Muchachos Observatory in La Palma, and the 70 cm telescope operated at the Babelsberg Observatory, Potsdam, Germany, by the AIP. The data presented here were obtained in part with ALFOSC, which is provided by the Instituto de Astrofisica de Andalucia (IAA) under a joint agreement with the University of Copenhagen and NOTSA. EH acknowledges support from the Spanish MINECO through grant ESP2014-57495-C2-2-R. VSD and ULTRACAM are supported by STFC. This research has made use of the SIMBAD data base and VizieR catalogue access tool, operated at CDS, Strasbourg, France, and of the NASA Astrophysics Data System (ADS). We thank the anonymous referee for a constructive review.

REFERENCES

Adams E. R., Dupree A. K., Kulesa C., McCarthy D., 2013, AJ, 146, 9
Bean J. L., Miller-Ricci Kempton E., Homeier D., 2010, Nature, 468, 669
Claret A., 2000, A&A, 363, 1081
Claret A., 2009, A&A, 506, 1335
Claret A., Hauschildt P. H., Witte S., 2013, A&A, 552, A16
Csizmadia S., Pasternacki T., Dreyer C., Cabrera J., Erikson A., Rauer H., 2013, A&A, 549, A9
de Mooij E. J. W. et al., 2012, A&A, 538, A46
de Mooij E. J. W. et al., 2013, ApJ, 771, 109
Dhillon V. S. et al., 2007, MNRAS, 378, 825
Dragomir D., Benneke B., Pearson K. A., Crossfield I. J. M., Eastman J., Barman T., Biddle L. I., 2015, ApJ, 814, 102
Eastman J., Siverd R., Gaudi B. S., 2010, PASP, 122, 935
Espinoza N., Jordán A., 2016, MNRAS, 457, 3573
Fortney J. J., Shabram M., Showman A. P., Lian Y., Freedman R. S., Marley M. S., Lewis N. K., 2010, ApJ, 709, 1396
Fukui A. et al., 2013, ApJ, 770, 95
Gibson N. P., Aigrain S., Barstow J. K., Evans T. M., Fletcher L. N., Irwin P. G. J., 2013a, MNRAS, 428, 3680
Gibson N. P., Aigrain S., Barstow J. K., Evans T. M., Fletcher L. N., Irwin P. G. J., 2013b, MNRAS, 436, 2974 (G13)
Gillon M., Pont F., Moutou C., Bouchy F., Courbin F., Sohy S., Magain P., 2006, A&A, 459, 249
Hartman J. D. et al., 2011, ApJ, 742, 59
Huitson C. M. et al., 2013, MNRAS, 434, 3252
Jordán A. et al., 2013, ApJ, 778, 184
Knutson H. A., Charbonneau D., Noyes R. W., Brown T. M., Gilliland R. L., 2007, ApJ, 655, 564
Kreidberg L. et al., 2014, Nature, 505, 69
Lendl M., Gillon M., Queloz D., Alonso R., Fumel A., Jehin E., Naef D., 2013, A&A, 552, A2
Lendl M. et al., 2016, A&A, 587, A67
Mallonn M., Strassmeier K. G., 2016, A&A, 590, A100 (Paper I)
Mallonn M. et al., 2015a, A&A, 580, A60
Mallonn M. et al., 2015b, A&A, 583, A138
Mancini L. et al., 2013, MNRAS, 436, 2
Müller H. M., Huber K. F., Czesla S., Wolter U., Schmitt J. H. M. M., 2013, A&A, 560, A112
Nascimbeni V., Piotto G., Pagano I., Scandariato G., Sani E., Fumana M., 2013, A&A, 559, A32
Nascimbeni V. et al., 2015, A&A, 579, A113
Nikolov N. et al., 2014, MNRAS, 437, 46
Nortmann L., Palle E., Murgas F., Dreizler S., Iro N., Cabrera-Lavers A., 2016, preprint (arXiv:1604.06041) (N16)
Oshagh M., Santos N. C., Ehrenreich D., Haghighipour N., Figueira P., Santerne A., Montalto M., 2014, A&A, 568, A99
Poddaný S., Brát L., Pejcha O., 2010, New Astron., 15, 297
Pont F., Sing D. K., Gibson N. P., Aigrain S., Henry G., Husnoo N., 2013, MNRAS, 432, 2917
Reif K. et al., 1999, in Blouke M. M., Williams G. M., eds, Proc. SPIE Conf. Ser. Vol. 3649, Sensors, Cameras, and Systems for Scientific/Industrial Applications. SPIE, Bellingham, p. 109
Seeliger M. et al., 2014, MNRAS, 441, 304
Sing D. K. et al., 2011a, MNRAS, 416, 1443
Sing D. K. et al., 2011b, A&A, 527, A73
Sing D. K. et al., 2015, MNRAS, 446, 2428
Sing D. K. et al., 2016, Nature, 529, 59
Southworth J., 2008, MNRAS, 386, 1644
Southworth J., 2011, MNRAS, 417, 2166
Southworth J., Maxted P. F. L., Smalley B., 2004, MNRAS, 351, 1277
Southworth J., Smalley B., Maxted P. F. L., Claret A., Etzel P. B., 2005, MNRAS, 363, 529
Southworth J. et al., 2009, MNRAS, 399, 287
Southworth J., Mancini L., Maxted P. F. L., Bruni I., Tregloan-Reed J., Barbieri M., Ruocco N., Wheatley P. J., 2012, MNRAS, 422, 3099
Stevenson K. B., 2016, ApJ, 817, L16
Stevenson K. B., Bean J. L., Seifahrt A., Désert J.-M., Madhusudhan N., Bergmann M., Kreidberg L., Homeier D., 2014, AJ, 147, 161
Strassmeier K. G. et al., 2004, Astron. Nachr., 325, 527
Teske J. K., Turner J. D., Mueller M., Griffith C. A., 2013, MNRAS, 431, 1669
Weber M., Granzer T., Strassmeier K. G., 2012, in Nicole M. R., Chiozzi G., eds, Proc. SPIE Conf. Ser. Vol. 8451, Software and Cyberinfrastructure for Astronomy II. SPIE, Bellingham, p. 84513H
Winn J. N. et al., 2008, ApJ, 683, 1076
Zhao M. et al., 2014, ApJ, 796, 115

APPENDIX: FIGURE OF THE RE-ANALYSED LITERATURE LIGHT CURVES

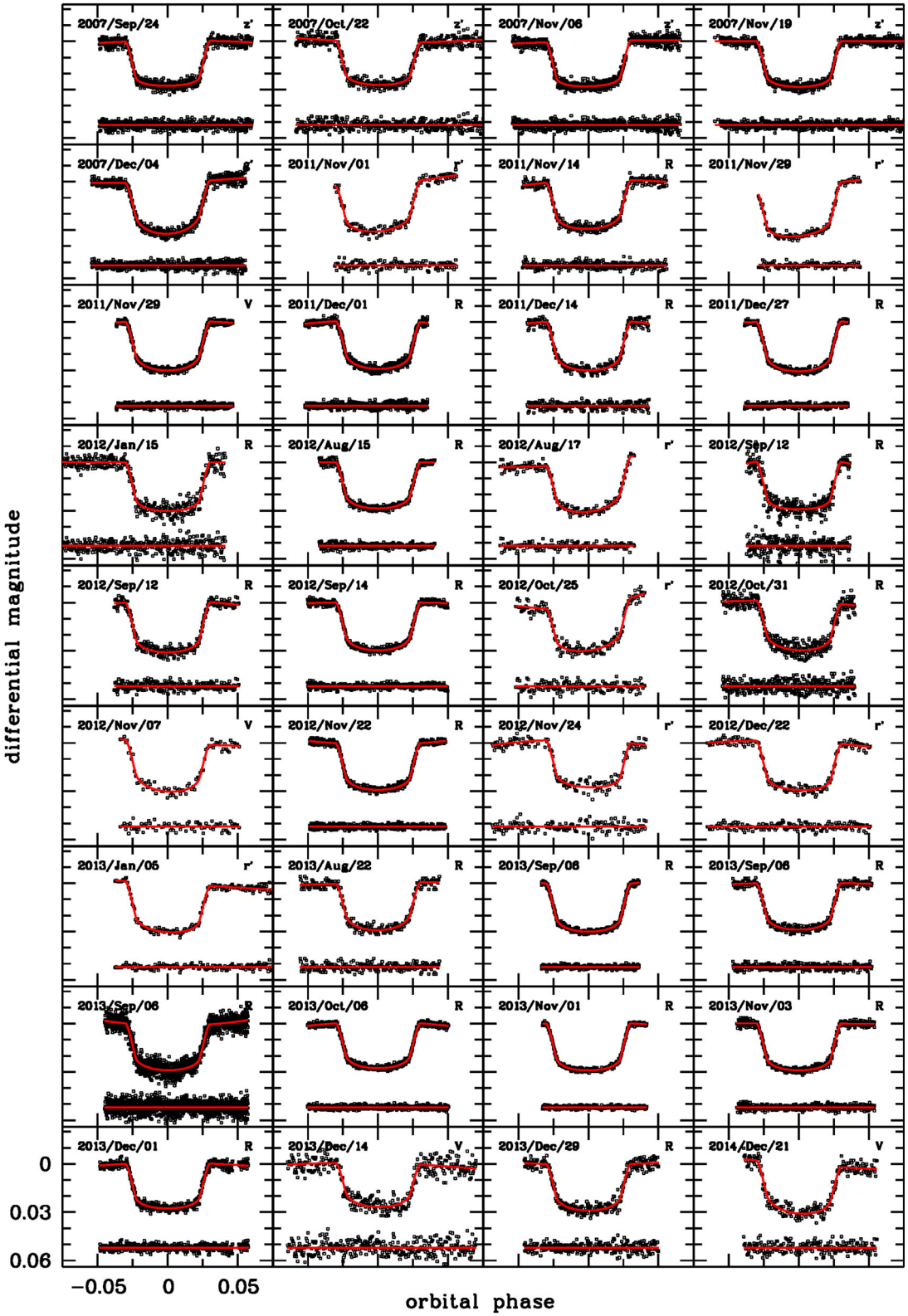

Figure A1. All literature light curves re-analysed in this work. The red solid line denotes the individual best-fitting model, the resulting parameter values are given in Table 2. Below the light curves, their corresponding residuals are shown. The scale of all panels is identical with the tickmarks labelled in the lower left.

This paper has been typeset from a TEX/LATEX file prepared by the author.